Stripe patterns: Role of initial state and boundary conditions

Ashwani K. Tripathi and Deepak Kumar*
School of Physical Sciences, Jawaharlal Nehru University, New Delhi 110067, India
(Received 3 April 2014; published 26 August 2014; corrected 29 August 2014)

This paper presents results on stripe patterns by numerical solution of the Swift-Hohenberg equation. The focus is on the role of initial state and boundary conditions. We choose initial states which generate simple defect configurations and study their evolution. Various classes of defects are identified and their motion and relaxation is studied numerically. We first study the dynamics of a straight front and present a comparison of numerical results with some analytical results. We then study the domain-wall dynamics in configurations containing two and three domains and identify some mechanisms of their relaxation. Rates of domain-wall relaxation depend on several features like incommensuration, dislocations and orientations in neighboring domains, in addition to the curvature of the walls. For a generic class of domain walls the relaxation process has an intrinsic frustration which leads to generation of dislocations. This process also generates stripe curvature thereby making relaxation nonmonotonic. We have also generated some other topological defects and studied their evolution and the effect of boundary conditions on their stability.

DOI: 10.1103/PhysRevE.90.022915 PACS number(s): 89.75.Kd, 47.54.−r, 64.60.De, 64.60.Cn

I. INTRODUCTION

Our understanding of patterns in a large number of physical, chemical, and biological situations has advanced considerably in the past 60 years or so. Several texts [1,2] and review articles [3–5] have covered these developments in recent years. The modeling of the phenomena in terms of partial differential equations for a few coupled fields has proved to be very rewarding. One of the most studied examples of this being the patterns of fluid convection, where equations for the velocity and temperature fields provide a quantitative description of the occurrence and evolution of the observed patterns.

Though many patterns form out of equilibrium, here we are concerned with situations where the evolution is towards steady states which have spatial periodicity. The evolution of such patterns can be described in terms of an appropriate free-energy functional. In particular we study here stripe patterns in two dimensions, whose common features are well described by the Swift-Hohenberg equation (SHE) [6], which is

$$\frac{\partial \psi(\vec{r},t)}{\partial t} = \left[\epsilon - \xi_0^4\left(\nabla^2 + q_0^2\right)^2\right]\psi(\vec{r},t) - \psi^3(\vec{r},t). \quad (1)$$

The linear analysis shows that for $\epsilon < 0$ a structureless uniform state with $\psi(\vec{r}) = 0$ is stable. For $\epsilon > 0$ this state becomes unstable to perturbations of wave vectors whose magnitudes lie in the range $q_0^2 - \sqrt{\epsilon}/\xi_0^2 < q^2 < q_0^2 + \sqrt{\epsilon}/\xi_0^2$. Though in two dimensions, planforms such as stripes, parallelograms, hexagons, etc. can occur, the above model gives rise to complex stripe patterns, which can locally be written in the approximate form

$$\psi(\vec{r},t) = A\,\cos(\vec{q}\cdot\vec{r} + \phi). \quad (2)$$

In a typical pattern-forming system as a control parameter is varied across a threshold, small domains with parallel and nearly straight stripes form first and such patterns coarsen with time. This process has been studied in a large number of papers [7–21]. This is similar to coarsening in systems with uniform order parameters, which is a well-studied subject with a rather long history [22–24], for example systems described by time-dependent Ginzburg-Landau equations. A major role in understanding these processes has been played by two concepts. First is the scaling hypothesis, which states that at late times the domain patterns differ statistically only through a time-dependent length scale. More concretely, for a scalar order parameter $u(\vec{r},t)$, the correlation function $C(\vec{r},t) = \langle u(\vec{x}+\vec{r},t)u(\vec{x},t)\rangle$, where brackets denote averaging over initial states, is given by

$$C(\vec{r},t) = \tilde{C}(\vec{r}/L(t)), \quad (3)$$

where the length scale $L(t) \propto t^n$ grows as a power law in time. Similar statements can be made for order parameters of other kinds. An important goal of the earlier studies has been to establish the scaling and determine the exponent n for different kinds of order parameters and different kinds of dynamics viz. those which conserve or do not conserve the order parameter. The second concept is that the late stage slow dynamics is largely governed by defects viz. domain walls, vortices in two dimensions (2D) (vortex lines in 3D), disclinations, dislocations, etc. Some of these are topological defects and their relaxation governs the value of the index n. The nature of defects in a system crucially depends on the order-parameter manifold [25–27].

The same concepts have been used to understand the coarsening of stripes and other spatially periodic patterns [7–9,11–19,21]. However, there are important differences. First, the scaling concept is based on the key assumption that a single length scale $L(t)$ characterizes the order, Eq. (3). This may not hold here as the order parameter has several components which may have different evolutions, Eq. (2). Secondly, the stripe patterns rarely evolve to a fully ordered state consisting of a single domain of parallel stripes.

It is therefore important to recall some relevant features of the stripe order parameter (OP) which we summarize below [28]. This OP is characterized by an amplitude A, wave vector $\vec{q}$, which gives the periodicity and direction of stripes, and ϕ the phase of their undulations, Eq. (2). The amplitude A reaches its saturation value in the early part of the evolution, apart from defected regions. The magnitude of $\vec{q}$ lies in a small

*dk0700@mail.jnu.ac.in

band (we shall study the problem near threshold, i.e., for small positive ϵ). Thus in two dimensions the order parameter is characterized by two angles ϕ and θ giving the direction of $\vec{q}$. For stripes $(-\vec{q},2\pi-\phi)$ and $(\vec{q},\phi)$ are equivalent. The OP manifold is $P_1 \times P_1$ which is a two-dimensional torus in which (ϕ,θ) and $(2\pi-\phi,\theta+\pi)$ are identified. The fundamental group of the manifold is $Z \times Z_2$, so according to the standard topological analysis, defects in this system are characterized by $m,n/2$, where m,n are any two integers. These are winding numbers in ϕ and θ respectively corresponding to dislocations and disclinations.

However, as observed by Chen, Alexander, and Kamien [28], such a classification fails here, as no disclinations with winding number greater that $+1$ can occur in a stripe system. This is due to the spatial coupling of $\vec{q}$ with phase ϕ as $\vec{q} = \vec{\nabla}\phi$. The system has only one Goldstone mode corresponding to phase relaxation (ϕ) but no mode for orientational relaxation (θ). This allows for sharp domain walls which are seen frequently in stripe patterns.

Another feature to be recalled for periodic or crystalline patterns in 2D is that the two components, phase order and orientational order, associated with the positional order are not tied to each other. Nelson and Halperin [29] showed that due to thermal fluctuations the system loses its phase order but not the orientational order above a certain temperature T_1, while the latter order is lost at a higher temperature T_2. Both the transitions are caused by defects. The phase order is destroyed by proliferation of free dislocation which can occur above T_1, while the orientational order is destroyed by free disclinations which occur above T_2. Toner and Nelson [30] studied the effect of thermal fluctuations specifically for the stripe order and argued that here a free dislocation has finite energy and the phase order is lost at any nonzero temperature due to their finite density. Dislocations do not disrupt the long-range orientational order which survives to a temperature at which free disclinations can occur.

The coarsening process in stripe systems is understandably more complex due to the presence of several types of defects described above. These relax and translate at different rates and affect order parameter through dephasing of translational phase and angular correlations in different ways. The previous studies [7–9,11–16,18,19,21] have disentangled many of these features, yet to our mind some issues need further clarifications. Since patterns emerging from a random initial state have interplay of several factors together, we have chosen to consider some simple initial states which together with boundary conditions allow study of patterns with simple configurations of defects.

The evolution of patterns in large domains from well-defined initial states raises interesting questions regarding symmetry breaking. When the equations governing the dynamical evolution have the symmetry which permits a number of ordered states within the order parameter manifold, the eventual emergence of a steady pattern involves a selection caused by the initial state together with boundary conditions. What are the parameters that select the order parameter of the emergent pattern? Since the states that emerge are rarely pure, the above question should be supplemented by the following. Under what conditions do certain defects or defect textures appear and which parameters can be used to predict their occurrence? Thus it is useful to understand the role of initial state and the boundary conditions in the selection of order parameter and other aspects related to defects in simpler situations.

In addition to numerical studies we also obtain an approximate time-dependent solution which shows explicit dependence on the initial state. Such studies were first done on the time-dependent Ginzburg-Landau equation for the scalar order parameter [31] and Fisher equation [32,33]. The earlier solutions based on a singular perturbation analysis [34] have proved useful for analyzing motion of fronts in one dimension and some features of time-dependent structure factor in these systems. Elder and Grant [35] applied this technique to pattern-forming systems and found a good account of the motion of the front in one dimension and averaged structure factor.

We apply this method in a somewhat different way. First we apply it to situations where single domain patterns form, aside from effects accruing from boundary conditions. Here also one needs to determine for a given initial state the values of $\vec{q}$ and ϕ that would eventually emerge. Since the initial states contain no stripes this is a nontrivial question. We present such a selection criterion based on linear evolution and show how it works for the single-domain patterns and how these patterns are modified by boundary conditions. One would like to extend the above considerations to situations where a specified set of topological defects occur, i.e., determine characteristics of the initial state that selects such topological features. However, we are not able to give criteria for even the case of single defects, but we do provide examples of initial states which produce specified defects.

This paper is organized as follows. In Sec. II we present the singular perturbation technique applied to the simplest case of a single domain pattern. Comparison between singular perturbation results and numerical solutions is discussed in Sec. III. In the following two sections we report numerical simulations on Swift-Hohenberg equation. In Sec. IV, we focus on the relaxation and motion of domain walls. We study initial states which evolve into few domains in simple configurations. We present detailed dynamical results in a few cases and identify features that occur commonly. In Sec. V, we generate isolated disclinations and study their growth and stability to boundary conditions. We conclude by summarizing our results in Sec. VI.

II. SINGULAR PERTURBATION THEORY FOR SINGLE DOMAIN PATTERNS

In order to extend the singular perturbation theory (SPT) for SHE, two additional physical points need to be considered. First is that there are two length scales, one corresponding to the periodicity of the pattern and the second to the scale over which the order parameter varies in space, say, around a defect or near a boundary. The singular perturbation method as originally formulated is suitable for fields which vary slowly in space. Therefore, we use the amplitude equation which describes how the amplitude of the stripe oscillations varies over a length scale much larger than the wavelength of the stripe pattern [36,37]. The second point is that this procedure requires a linear solution about which the perturbation theory

is developed. For this one needs to specify the wave-vector direction and phase of the solution, which are also the parameters of the eventual pattern that emerges.

Our criterion of selection of direction $\vec{e}$ and phase ϕ of stripe patterns uses linear analysis, according to which the fastest growing mode occurs at wave number $q = q_0$. We assume that the final stripe pattern has the wave vector $\vec{q} = q_0\vec{e}$ and phase ϕ. Now given an initial state $\psi(\vec{r},0)$, we define the following quantity in an infinite domain:

$$G(\vec{e},\phi) = \int_{-\infty}^{\infty}\int_{-\infty}^{\infty} \psi(\vec{r},0)\cos(q_0\vec{e}\cdot\vec{r}+\phi)d^2r. \quad (4)$$

The direction $\vec{e}$ and phase ϕ of the final stripe pattern is determined by maximizing $G(\vec{e},\phi)$ with respect to these arguments.

For stripe patterns $\psi(\vec{r},t)$ is written as

$$\psi(\vec{r},t) = A(\vec{r},t)e^{iq_0\vec{e}\cdot\vec{r}} + \text{c.c.}, \quad (5)$$

where $A(\vec{r},t)$ is a complex amplitude which varies slowly on the scale of $2\pi/q_0$. For the Swift-Hohenberg equation ($\xi_0 = 1$), the amplitude equation is [36,37]

$$\frac{\partial A}{\partial t} = \epsilon A + 4q_0^2(\vec{e}\cdot\vec{\nabla})^2 A - 3|A|^2 A. \quad (6)$$

The singular perturbation analysis [31] yields an approximate solution of Eq. (6) to be

$$A(\vec{r},t) = \frac{\sqrt{\epsilon}A^0(\vec{r},t)}{[\epsilon + 3|A^0(\vec{r},t)|^2]^{1/2}}, \quad (7)$$

where $A^0(\vec{r},t)$ is the solution of the linear part of Eq. (6). Its Fourier transform $\tilde{A}^0(\vec{k},t)$ is given by

$$\tilde{A}^0(\vec{k},t) = \exp\left\{\left[\epsilon - 4q_0^2(\vec{e}\cdot\vec{k})^2\right]t\right\}\tilde{A}(\vec{k},0) = e^{\gamma_k t}\tilde{A}(\vec{k},0). \quad (8)$$

$\tilde{A}(\vec{k},0)$ is to be determined from the initial condition $\psi(\vec{r},0)$. The Fourier transform of the initial field using Eq. (5) can be written as

$$\tilde{\psi}(\vec{k},0) = \tilde{A}(\vec{k}+\vec{q}_0,0) + \tilde{A}^*(\vec{k}-\vec{q}_0,0). \quad (9)$$

This equation can be used to derive the following recursion formula for $\tilde{A}(\vec{k},0)$:

$$\begin{aligned} 2\tilde{A}(\vec{k},0) = \sum_{n=0}^{N}(-1)^n\{&\tilde{\psi}[\vec{k}-(-1)^n(2n+1)\vec{q}_0,0] \\ &+ \tilde{\psi}^*[\vec{k}+(-1)^n(2n+1)\vec{q}_0,0]\} \\ &+ \{\tilde{A}[\vec{k}-2(N+1)\vec{q}_0,0] + \tilde{A}[\vec{k}+2(N+1)\vec{q}_0,0]\}. \end{aligned} \quad (10)$$

Since the amplitude $A(\vec{r},t)$ varies slowly in space, its Fourier transform has significant value only for small values of k. By neglecting $\tilde{A}[\vec{k}\pm 2(N+1)\vec{q}_0,0]$ we can use the relation to obtain $\tilde{A}(\vec{k},0)$ with increasing accuracy by raising the value of N. Now the linear solution is

$$\begin{aligned} A^0(\vec{r},t) = \int \frac{d^2k}{(2\pi)^2}e^{\gamma_k t}e^{-i\vec{k}\cdot\vec{r}}\int d\vec{r}'\psi(\vec{r}',0)[&e^{-i\vec{q}_0\cdot\vec{r}'} - e^{3i\vec{q}_0\cdot\vec{r}'} \\ &+ e^{-5i\vec{q}_0\cdot\vec{r}} - \cdots + (-1)^N e^{-i(-1)^N(2N+1)\vec{q}_0\cdot\vec{r}}]. \end{aligned} \quad (11)$$

The SPT solution for $\psi(\vec{r},t)$ is obtained by combining Eqs. (5) and (7).

III. COMPARISON OF SPT WITH NUMERICAL RESULTS

We have compared the singular perturbation theory (SPT) result with numerical solution (NS) for the initial states which give rise to single-domain states with no defects. All the numerical results of SHE are computed for $\epsilon = 0.1$ and $q_0 = 1$ on a square lattice 1025×1025 with $\Delta x = 0.2$ and $\Delta t = 0.0001$. We choose initial states which have gradients only along one direction and parallel to one of the boundaries. Periodic boundary conditions are used. The first initial condition we consider is

$$\psi(x,y,0) = \begin{cases} 1 & \text{if } \ x_0 - a \leqslant x \leqslant x_0 + a, \\ 0 & \text{otherwise.} \end{cases} \quad (12)$$

According to the pattern selection criterion Eq. (4) the wave vector of the final stripe pattern will be in x direction. The comparison of the SPT solution for $N = 3$ with numerical solution of SHE at three times is shown in Fig. 1. Results compare well after a time of 40 units. The selected wave vector is 1.01.

From the above results the front speed can be calculated as a function of time. The front position $x(t)$ is shown as dots in Fig. 1(d). The front position is taken to be the position where the stripe amplitude is half of its maximum value. This result is compared with the theoretical analysis [38,39]. The result for the speed of the front moving from the stable stripe state into the unstable uniform state for SHE is

$$v(t) = v^* - \frac{3}{2\lambda^* t}, \quad (13)$$

where the asymptotic front speed v^* is given by

$$v^* = \frac{4}{3\sqrt{3}}(\sqrt{1+6\epsilon}+2)(\sqrt{1+6\epsilon}-1)^{1/2}, \quad (14)$$

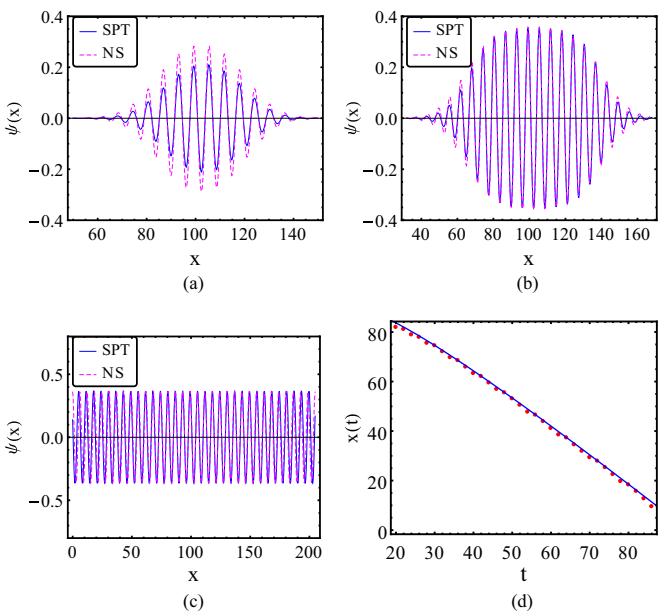

FIG. 1. (Color online) Comparison of numerical simulation to singular perturbation theory for the initial condition Eq. (12) is shown at different times: (a) $t = 20$, (b) $t = 40$, and (c) $t = 120$. Panel (d) shows positions of the front $x(t)$ with time as dots. The continuous line is the fit according to Eq. (13).

and λ^* is a parameter of the theory whose value is adjusted using numerical results. The result using Eq. (13), shown as a full line, fits very well with the numerical data. Note that the asymptotic speed measured is 1.33 ± 0.04, whereas Eq. (13) yields 1.29 and the SPT yields 1.26.

In order to test the robustness of SPT we consider a perturbed step function of the form

$$\psi(x,y,0) = \begin{cases} 1 & \text{if} \quad x_0 - a \leqslant x \leqslant x_0 + a, \\ \alpha + \beta \sin(\mu x) & \text{if} \quad x_0 - 2a < x < x_0 - a \quad \text{and} \quad x_0 + a < x < x_0 + 2a, \\ 0 & \text{otherwise.} \end{cases} \tag{15}$$

We have done comparison for many values of α with $\beta = \mu = 0.1$. For a value of α close to unity the numerical results and SPT match well after an initial period. However, on increasing the perturbation, $\alpha = 0.5$, agreement between NS and SPT deteriorates (see Fig. 2). At early times there is mismatch in both the amplitude and the phase of the oscillations but at larger times the solution matches reasonably as SPT is expected to be good at large times. This is a limitation of the SPT. The Fourier transform of the initial state contains a spread of wave vectors, whereas in SPT only the fastest growing mode is treated well. The deviations from the selected wave vector $\vec{q}_0$ lead to phase deviations which are only partially corrected at long times. The wave-vector spread increases as α decreases.

We have investigated other initial states to test the criterion for wave-vector selection. Even with simplest initial states the boundary conditions lead to nucleation of more than one grain, but the criterion can be seen to be satisfied at a local level and at times before the boundary effects come into play. In the next sections we deal with more complicated boundary conditions in which the nucleation occurs at boundaries as well as regions of large gradients of ψ. Accordingly, several fronts move simultaneously and overlap quickly. The SPT which is built around a single solution $\cos(\vec{q} \cdot \vec{r} + \phi)$ needs to be used in different regions with different directions of $\vec{q}$. We have not been able to implement this program successfully yet. Therefore, only numerical studies of the Swift-Hohenberg equation (SHE) are shown in the following sections.

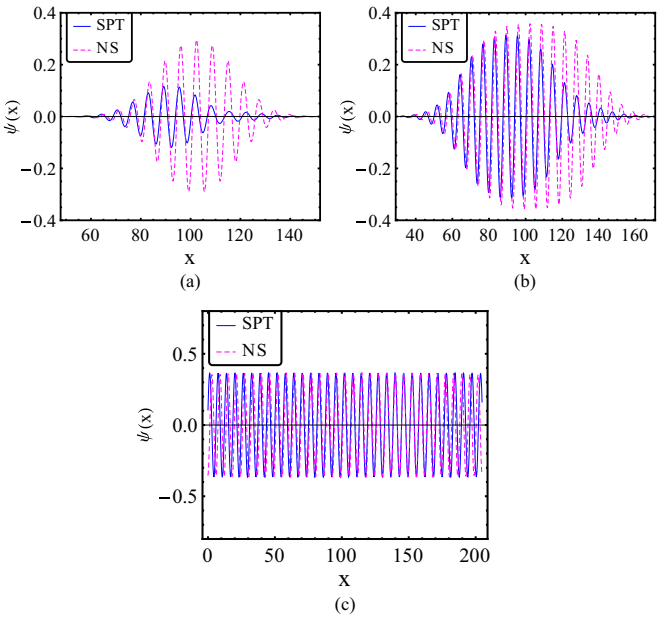

FIG. 2. (Color online) Comparison of numerical simulation to singular perturbation theory for the initial condition given by Eq. (15) with $\alpha = 0.5$ is shown at different times: (a) $t = 20$, (b) $t = 40$, and (c) $t = 120$.

IV. STRUCTURE AND DYNAMICS OF DOMAIN WALLS

In this section we study some initial states which evolve into simple configurations of domains with two or three domain walls. Domain walls are the dominant defects in stripe configurations and play a significant role in the relaxation and the coarsening process. In this and the following sections the symmetry breaking involved in pattern formation is due to the initial state and boundary conditions. In order to identify defects and quantify the dynamical process we have used numerical procedures given by Qian and Mazenko [18] and extended them in some ways. This is summarized in the next subsection.

A. Numerical procedure

In this procedure one identifies the grain boundaries and isolated defects by examining the spatial variation of a field $\vec{B}$. The field $\vec{B}$ is constructed from the director field $\hat{n}$ in the following way:

$$\hat{\mathbf{n}} = \frac{\nabla\psi}{|\nabla\psi|} = (\cos\theta, \sin\theta) \tag{16}$$

and

$$\begin{aligned} B_x &= \cos\chi = n_x^2 - n_y^2, \\ B_y &= \sin\chi = 2n_x n_y, \end{aligned} \tag{17}$$

where $\chi = 2\theta$. Then these fields are smoothened over the lattice using the iterative process

$$f_{n+1}(i,j) = \frac{1}{2} f_n(i,j) + \frac{1}{8} \sum_{(i',j') \in NN} f_n(i',j'). \tag{18}$$

This smoothening suppresses small fluctuations away from the defects. Next we calculate the quantity $D(\vec{x})$ defined as

$$D(\vec{x}) = \sum_{\alpha,\beta} (\nabla_\alpha B_\beta)^2 = \sum_{\alpha} (\nabla_\alpha \chi)^2. \tag{19}$$

Due to the periodic nature of χ some care is needed to calculate its derivative. We define the difference $(\chi_{i+1,j} - \chi_{i-1,j})$ as

$$\begin{aligned} \chi_{i+1,j} - \chi_{i-1,j} = \min(&|\chi_{i+1,j} - \chi_{i-1,j}|, |\chi_{i+1,j} - \chi_{i-1,j} \\ &+ 2\pi|, |\chi_{i+1,j} - \chi_{i-1,j} - 2\pi|). \end{aligned} \tag{20}$$

Once we have calculated $D(\vec{x})$, a particular site is identified as defect if $4(\Delta x)^2 D(\vec{x})$ is greater than a threshold D_0 [18]. We have taken $D_0 = 2$. After picking out all such sites, the next step is to identify them either as point defects or belonging to an extended structure like a grain boundary. For this purpose a filter R is defined such that when distance between two defect sites is less than or equal to R, they are part of the same structure. We have used the cluster multiple labeling method of Hoshen and Kopelman [40] to pick out these clusters and their sizes. In order to distinguish between point defect and grain boundary, we define a filter l_0 such that, when a size of a structure is less than l_0, the structure corresponds to a point defect; otherwise, it is a grain boundary. Both R and l_0 are fixed by trial after corroborating the defect identification visually. Point defects are further classified into dislocations and disclinations by calculating the line integral of $\chi(\vec{x})$ over a counterclockwise path around the mass center of the point defect:

$$\oint \frac{\partial \chi}{\partial s} ds. \tag{21}$$

In our computation we have taken a 16×16 square as the closed contour. If the integral is zero, then the given point defect is dislocation. If it is close to $2\pi m$, it is a disclination of strength $m/2$.

B. Domain walls: Two domains

In order to generate configurations with two or three domains in cells with periodic boundary conditions, it is convenient to take an initial state of the form

$$\psi(\vec{r},0) = \frac{1}{1 + \exp[\vec{n} \cdot (\vec{r} - \vec{r}_0)/\xi]}. \tag{22}$$

Depending on the value of ξ and $\vec{n}$ this function allows gradients and nucleation along the line $\vec{n} \cdot (\vec{r} - \vec{r}_0)$ and along the edges of the square domain. For large ξ of the order of the domain size, the case we consider first, the nucleation occurs dominantly at the boundaries. This leads to two domains. Here we also examine the effect of incommensuration by studying two cases in which the lattice period is commensurate or incommensurate with the stripe period. We shall see that the incommensuration introduces dislocations and changes the evolution considerably.

First in Fig. 3 we show patterns evolving for the initial state with $\xi = 1000$ and $\vec{n} = (1, \sqrt{3})/2$ for a commensurate 512×512 lattice with $\Delta x = \pi/4$. $\vec{r}_0$ is taken to be the center of the square cell in this and all the following simulations. Here the pattern evolves rapidly into two domains with stripes parallel to the two square edges and no other defect. The first panel shows the initial state.

In order to describe the time dependence of the annihilation process of the domain we first present the results for the evolution of the total number of defects $N_D(t)$ and the excess free energy $\Delta F(t)$ in Fig. 4. Here t is measured from the time the domain wall has formed. The inset of Fig. 4(b) also shows a plot of $\Delta F(t)$ with $N_D(t)$. This shows a linear dependence of the two quantities, though $N_D(t)$ shows considerable fluctuation on a shorter time scale. These curves can be fitted well to a polynomial of the form $a + bt + ct^2 + dt^3$;

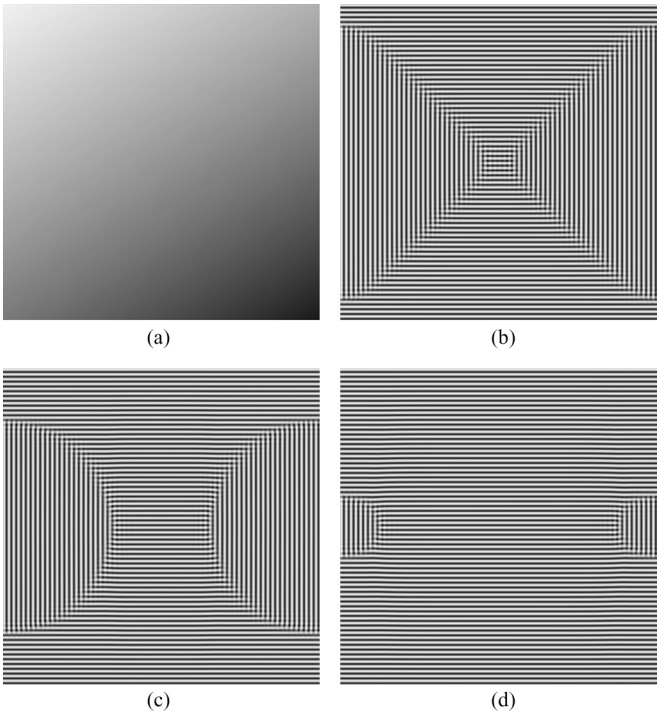

FIG. 3. Four panels show patterns evolving from the initial condition in Eq. (22) at different times: (a) $t = 0$, (b) $t = 300$, (c) $t = 3000$, and (d) $t = 12\,000$. Parameters of the initial state are $\xi = 1000$, $\vec{n} = (1/2, \sqrt{3}/2)$, and $\vec{r}_0$ is the center of the square cell.

however, such a fit yields little insight into the mechanism involved. We argue that the decay process is autonomous: $d(\Delta F)/dt = f(\Delta F)$. In Fig. 5(a) the plot of $d(\Delta F)/dt$ with ΔF is shown. There is distinct difference between the late and early time stages. For the late stage $f(\Delta F) \approx -k(\Delta F)^{-1.08}$, while in the early stage decay rate increases rapidly with ΔF.

The motion of the domain wall is tracked by looking at certain points on the wall. Figure 5 shows the motion of end points $X_{\max}$ and $Y_{\max}$ of the lower left of the domain wall. These points move horizontally and vertically respectively and have identical time dependence which is similar to the free energy. We tracked other points on the wall as well. All the points show the same time dependence in this case. A wall is characterized

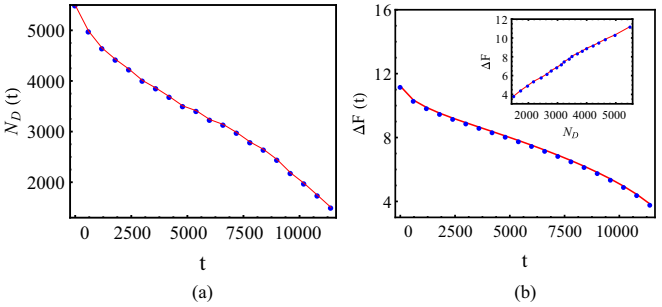

FIG. 4. (Color online) (a) Evolution of the total number of defect points $N_D(t)$ and (b) the excess free energy $\Delta F(t)$ with time. The time t is measured from the time the domain wall is formed. The inset shows a plot of ΔF with N_D. Continuous lines are a guide to the eyes.

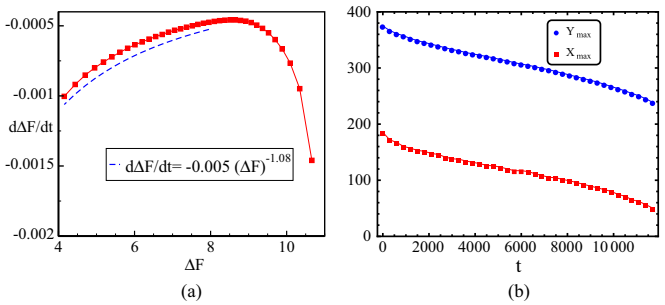

FIG. 5. (Color online) (a) Plot of $d(\Delta F)/dt$ with ΔF. The dotted line is the power-law fit at the late stage. (b) Motion of end points $X_{\max}$ and $Y_{\max}$ of the lower left of the domain wall in Fig. 3(c).

by two angles θ_1 and θ_2 that the stripes on the two sides make with the wall. Since the stripe amplitude vanishes on the wall, one can argue following Cross [41] that the wall energy per unit length should be $\propto \epsilon^{3/2}\xi_0(|\cos\theta_1| + |\cos\theta_2|)$. For the wall here both angles vary from 0 to $\pi/2$, and the curvature of the wall also varies considerably over its length. The speed of a wall in the absence of dislocations or other defects does not seem to depend on these factors.

In this case where the two domains consist of perpendicular stripes, steps of annihilation can be easily discerned. We consider the motion near $X_{\max}$, where a short vertical stripe annihilates to allow the advance of horizontal stripes. In Figs. 3(c) and 3(d) one sees that the vertical stripe evolves into spots equispaced at distance of $2\pi/q_0$ to which the horizontal stripes join in. In other parts the dissociation of the vertical stripes occurs only in portions near the wall which allows horizontal stripes to advance. The above results for two domains are not specific to one initial state. Similar domains arise with other initial states; for example, the state given in Eq. (24) gives rise to two domains without any other defects for large values of ξ. Here again one finds a similar behavior except when the domain wall becomes small.

Next we come to the incommensurate case. Figure 6 shows four panels of evolution at times indicated. The initial two domains are formed rapidly, but the evolution shows three distinct stages. In the first stage $10 < t < 20\,000$ domain-wall motion remains considerably slower, particularly in x direction. At $t \approx 20\,000$ a pair of horizontal dislocations is nucleated [see Fig. 6(c)] and thereafter the wall moves at a speed comparable to the commensurate case. The domain is annihilated and in the final stage the dislocation pair is annihilated. The relative speed of dislocations is constant all through.

Figures 7(a) and 7(b) show the evolution of the total number of defect sites $N_D(t)$ and the excess free energy $\Delta F(t)$ with time. Time dependences in both cases are similar but the decay rates are halved compared to the commensurate case. The inset of Fig. 7(b) shows the linearity of $\Delta F(t)$ with $N_D(t)$. We again analyze it by considering the plot of $d(\Delta F)/dt$ with ΔF. This plot is quite different indicating the strong effect of incommensuration. Here $f(\Delta F)$ shows distinct steps and jumps in the force. Within the scenario for the domain annihilation presented above, this is suggestive of the following. As the vertical stripes dissociate into spots,

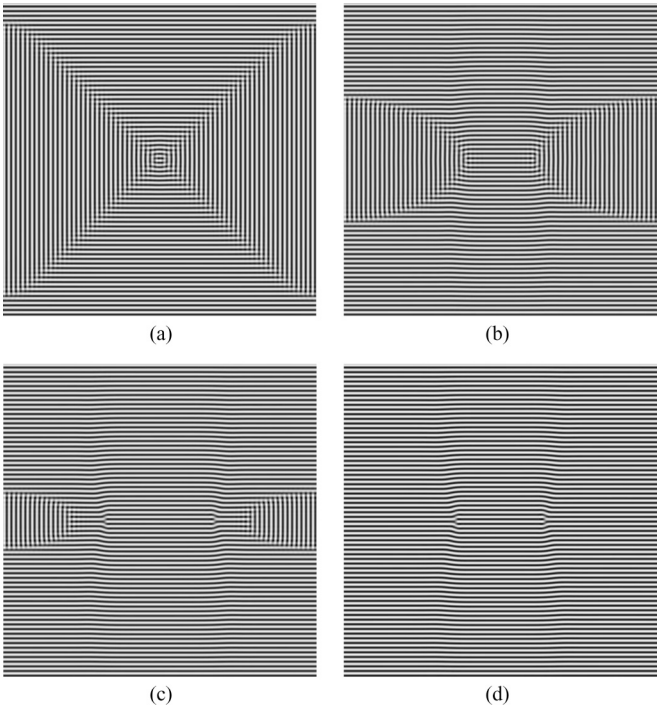

FIG. 6. Patterns evolving from the initial condition of Fig. 3 for incommensurate 513×513 lattice with $\Delta x = 0.8$ at different times: (a) $t = 300$, (b) $t = 12\,000$, (c) $t = 21\,000$, and (d) $t = 30\,000$.

horizontal stripes join them through curved segments in order to accommodate an extra stripe in the middle, which eventually results in the dislocation pair. After the formation of dislocations, spots and stripes are commensurate and the wall moves more rapidly. Thus the generation of the dislocation pair releases structural frustration.

The incommensuration causes an anisotropic motion of the wall as seen in Fig. 6. So the motion of the end points and also some intermediate points of the domain wall were tracked. Figure 8(a) show the motion of end points $X_{\max}$ and $Y_{\max}$ of the lower left of the domain wall. The position along the X direction varies linearly in time, whereas the position in the Y direction varies as $t^{0.6}$. Figure 8(b) show the positions of two intermediate points. These show a similar difference in x and y directions as the end points.

We have also examined the spread of the wave number in the above two cases. For this purpose, we calculated the power spectrum of the order parameter $\psi(\vec{r},t)$ defined as

$$P(k,t) = \langle|\psi(\vec{k},t)|^2\rangle_{av}, \tag{23}$$

where the bracket denotes an angular average over $\vec{k}$. This is shown in Fig. 8(c) for the incommensurate case. The main peak occurs very close to $q_0 = 1.0$ and there is very little spread indicating that the wave vectors in two domains differ very little in spite of the presence of dislocations. This shows that the presence of dislocation does not change the magnitudes of k vector significantly. In this case it is difficult to relate the velocity of the dislocation to wave-vector deviation caused by the dislocation. However, the existence of the second peak at $k \approx 4.0$ is somewhat surprising. It is seen only in the incommensurate case, when both the dislocation and the

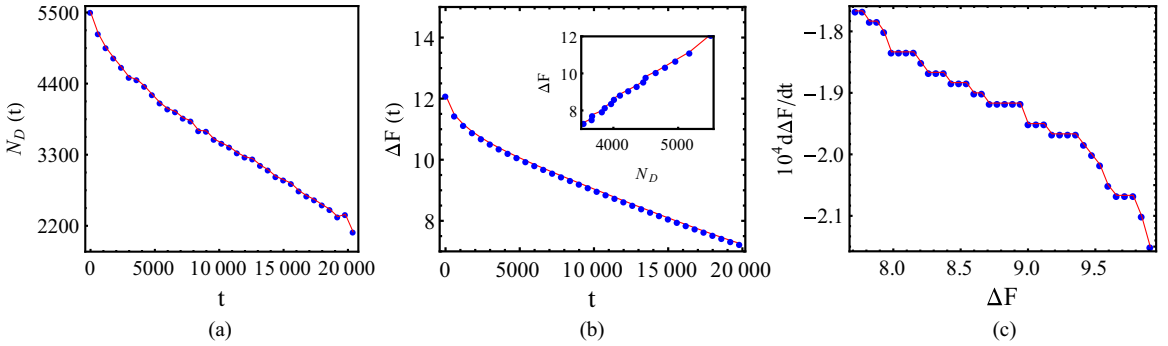

FIG. 7. (Color online) Evolution of (a) total number of defect points $N_D(t)$ and (b) excess free energy $\Delta F(t)$. (c) Plot of $d(\Delta F)/dt$ with ΔF. Continuous lines are a guide to the eyes.

grain boundary are present. It vanishes along with the grain boundary, and thus represents a short scale modulation of stripes caused together by the grain boundary and dislocation. The second peak is not seen for the commensurate lattice. The same calculation for the commensurate case again shows a single sharp peak at $q_0 = 1.03$.

C. Grain boundary: Three domains

In order to generate more complex configurations we decrease ξ in the initial condition given by Eq. (22). In this section we take the initial state with $\xi = 0.01$ and $\vec{n} = (\sqrt{3}/2, 1/2)$ as shown in Fig. 9(a). Now the nucleation occurs on three fronts: one front is along the line $\vec{n} \cdot (\vec{r} - \vec{r}_0) = 0$, while the other two fronts are due to periodic boundary conditions along horizontal and vertical directions. They occur along the portions of the boundaries where the fields at the opposite edges do not match. A stripe pattern of three domains in directions governed by gradients in these regions quickly emerges with somewhat wide walls, Fig. 9(b). At this stage the stripes are quite straight. The horizontal grain is the smallest and it shrinks in time $t = 10\,800$, which is much longer than the time for the development of stripes [Fig. 9(c)]. Between the other two domains there are two kinds of domain walls. One set of opposite walls are rather straight in which $\theta_1 \approx \pi/2$ and θ_2 is fairly acute. Such walls occur quite commonly in other simulations, which is because their energy $\propto(|\cos\theta_1| + |\cos\theta_1|)$ is lower. The other set of opposite walls are like low angle grain boundaries with both angles θ_1 and θ_2 small. These are somewhat broad and meandering with a high density of dislocations and small stripes lying between.

These two kinds of walls relax differently. The walls relax as stripes from two sides connect through a curved segment. For the straight walls this process is frustrated as the number of stripes ending on two sides are different. This is so, as the projected distance on the wall is $\lambda/\sin\theta$, one sees that the number of stripes hitting the wall from two sides is different when $\theta_1 \neq \theta_2$. Thus, as seen in Fig. 9(c), alternate stripes connect leaving a string of dislocations. In subsequent evolution, stripes in both domains become progressively wavy as if the local curvature from the connection site is diffusing [see Fig. 9(d)]. This also results in slow rotation of the wall which reduces the angle between the stripes on two sides. This process also leads to a slow reduction in the number of dislocations in the wall which occurs at the ends of the wall. However, the coarsening through these processes is not monotonic as new regions of disorder are introduced and curvature of stripes increases in some regions and decreases in others. The entire process is not completed till time $t = 210\,000$ [see Fig. 9(f)], though the number of domains is reduced to one as in some regions the curved stripes get smoothly connected.

The first step in the relaxation of the low angle walls is the annihilation of smaller stripes which interweave dislocations. The stripes from two sides cannot connect here as the curvature required will be rather large. So the relaxation occurs by annihilation of dislocations and rotation of walls locally. This process also causes a waviness of stripes as the local curvature

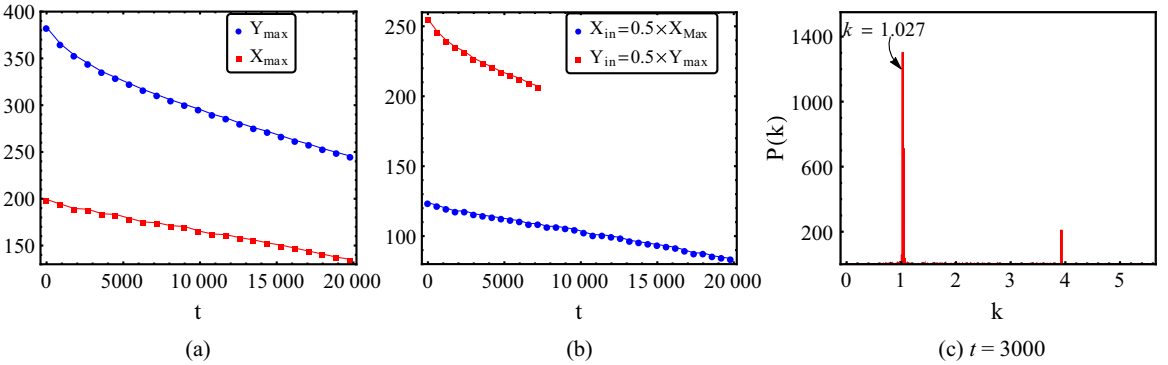

FIG. 8. (Color online) (a) Motion of end points X_{max} and Y_{max} of the left domain wall. (b) Motion of intermediate points X_{in} and Y_{in} of the left domain wall. Continuous lines are a guide to the eyes. (c) Power spectrum $P(\vec{k})$ vs k.

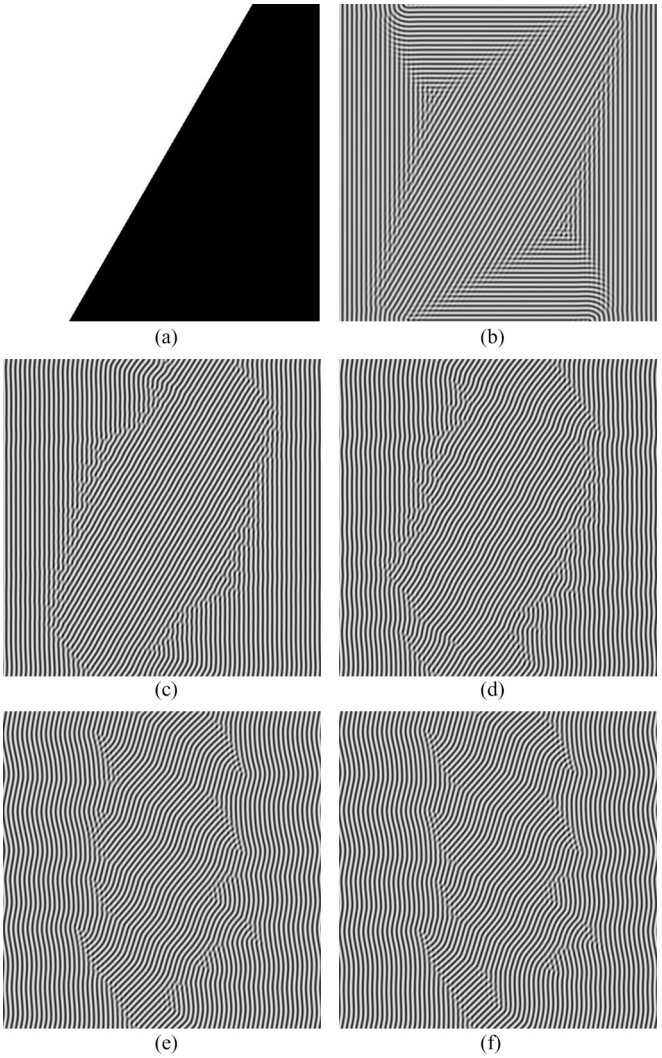

FIG. 9. Six panels show patterns evolving from the initial condition in Eq. (22) on a 513×513 lattice at different times: (a) $t = 0$, (b) $t = 300$, (c) $t = 10\,800$ and (d) $t = 30\,000$, (e) $t = 150\,000$ (f) $t = 210\,000$. Parameters of the initial state are $\xi = 0.01$, $\vec{n} = (\sqrt{3}/2, 1/2)$, and $\vec{r}_0$ is the center of the square cell.

is transported away. The defected regions diffuse and also reappear at another location. Notably defected regions which appear often have walls in which one angle is nearly $\pi/2$ (see Fig. 9), implying energy dissipation. So again some of these structures have frustration with regards to relaxation. These walls also do not relax till $t = 210\,000$ (see Fig. 9), the longest time of our simulation.

We have done many other simulations by varying the direction of $\vec{n}$ and ξ. The variation of $\vec{n}$ changes the sizes of the three domains seen above, but one sees similar general features. It seems that several processes quite distinct from the standard picture of curvature driven motion are operative and they have different time behavior and time scales. Further, whether a grain will annihilate seems to depend on the stripe orientations surrounding it, implying a global feature originating from long-range orientational order. In general a domain enclosed by a single domain is annihilated rather fast for a variety of shapes.

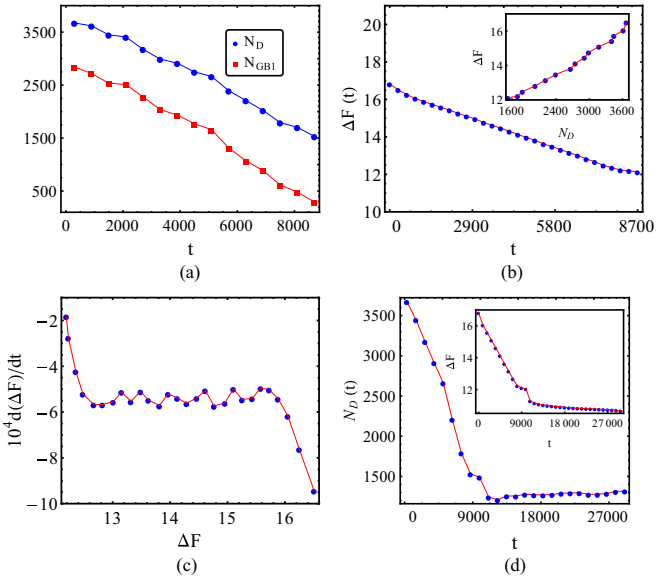

FIG. 10. (Color online) (a) Evolution of total number of defect sites $N_D(t)$ and number of defect sites $N_{GB1}(t)$ in the domain wall of horizontal stripes. (b) Early evolution of excess free energy $\Delta F(t)$. Inset show a plot of $\Delta F(t)$ with $N_D(t)$. (c) Plot of $d(\Delta F)/dt$ with ΔF at early times. (d) Evolution of total defect sites $N_D(t)$ over a longer range of time. Inset show a plot of $\Delta F(t)$ with t for the same range.

We substantiate some of these remarks quantitatively. First we study the small time regime ($t < 10\,000$) when three domains are present. The dynamics is dominated by the decay of the domain with horizontal stripes [see Figs. 9(b) and 9(c)] as this occurs at a faster time scale which is of the same order as the decay time of the domain in the commensurate case above. Figure 10(a) shows the decay behavior of the total number of defects $N_D(t)$, and defects $N_{GB1}(t)$ contained in this domain wall. Figure 10(b) shows the decay behavior of the excess free energy and the inset shows the variation of ΔF with $N_D(t)$. The defect numbers which are larger here show much more fluctuation. The free energy is expectedly somewhat smoother. The force curve shown in Fig. 10(c) is more or less constant apart from the initial and final states of the domain. For the long-time regime ($10\,000 < t < 30\,000$) shown in Fig. 10(d) one clearly sees that the defect population does not decrease and keeps fluctuating. On the other hand, the excess free energy does decrease very slowly in accordance with the picture described above.

Finally, we describe the time evolution of the stripe curvature. We evaluate the local curvature $C(\vec{x},t) = 2\pi|\nabla \cdot \vec{n}|/q_0$ in the entire region in which the stripes are formed using an amplitude filter [13,16]. The spatial average of stripe curvature $\bar{C}(t)$ is shown in Fig. 11(a). In the first phase when a domain is getting annihilated $C(t)$ decreases till $t = 10\,000$ (not shown). In the second phase $\bar{C}(t)$ increases as stripes across other walls connect and this local curvature diffuses leading to waviness along the length of involved stripes. This is followed by a regime in which the relaxation becomes very slow and frustrated. In Fig. 11(b) we show the curvature distribution $P(C,t)$ among sites with well formed stripes. The distribution broadens with time indicating that the stripes

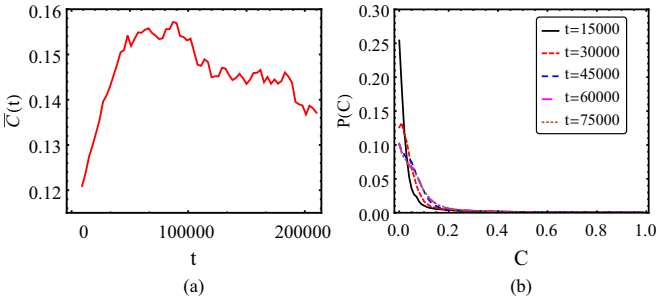

FIG. 11. (Color online) (a) Evolution of average stripe curvature with time. (b) The distribution of stripe curvature at various times.

are getting curved over larger regions with time. This sort of behavior for curvature seems generic in configurations where domain-wall relaxation is frustrated and the neighboring domains are not oriented in directions favorable to annihilation of the intervening domain.

V. GENERATION OF TOPOLOGICAL DEFECTS

In this section we study the evolution of initial states which have the topology of isolated defects. The motivation behind this study is to test the invariance of the topological properties of the order parameter through dynamical evolution. Topological properties of the order parameter can be studied only when some kind of order has been established in the system. However, the initial condition may not have the hint of this order and characteristic indices such as winding number may not be defined. Nevertheless, it seems physically possible to guess some initial states which lead to final states with a specified topological defect. We present some examples below.

A. Focus

A focus is the simplest of topological defects with winding number of +1. An initial state which generates a single focus is intuitively the one where the field is nonzero in a localized region small compared to the cell. So we have taken them to be Gaussian of the following form:

$$\psi(x,y,0) = \exp\left[-\frac{(x-x_0)^2}{\xi_x^2} - \frac{(y-y_0)^2}{\xi_y^2}\right]. \qquad (24)$$

In Fig. 12 we show results with $\xi_x = \xi_y = 28.6$. One sees from Fig. 12(b) that focus develops very rapidly covering the entire domain in a time $t = 600$. Thereafter the forcing due to boundaries is the main evolution which occurs through the formation of domain walls between focus and stripes compatible with periodic boundary conditions [see Figs. 12(c) and 12(d)]. The two sets of walls form across a diagonal where the boundary induced stripe direction is in conflict with focus. There are $\pi/2$ walls where one of the angles θ_1 or θ_2 is $\approx \pi/2$ in intermediate stages. Finally, some walls cannot annihilate without changing the winding number of the inner domain and so do not relax. The winding number of the configuration remains +1.

If the seed is made anisotropic with $\xi_x = 19.6$, $\xi_y = 28.6$, the focuslike stripe front moves more rapidly in the x direction

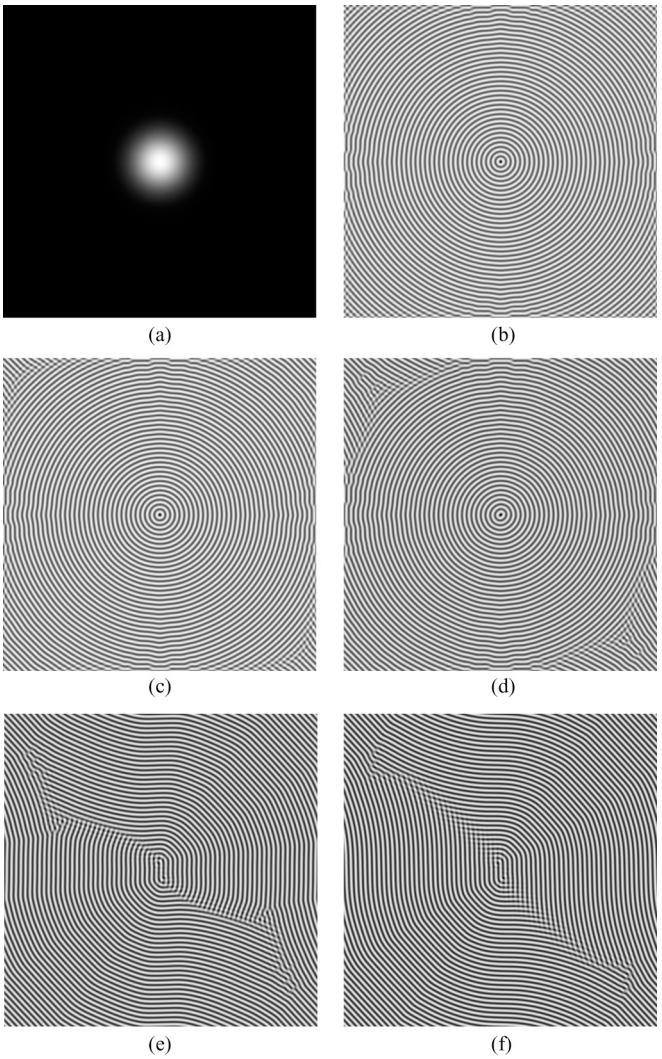

FIG. 12. Patterns evolving from the initial condition in Eq. (24) with $\xi_x = \xi_y = 28.6$ are shown at different times: (a) $t = 0$, (b) $t = 600$, (c) $t = 3000$, and (d) $t = 12\,000$. The last two panels show the late stage configurations for an anisotropic seed with $\xi_x = 19.6, \xi_y = 28.6$ at times (e) $t = 90\,000$ and (f) $t = 180\,000$.

and longer domain walls along the diagonal emerge. The late time configurations are shown in Figs. 12(e) and 12(f).

B. +1/2 disclination

In order to generate a convex $n = 1/2$ isolated defect, the angular part of the initial state is taken to be the static solution of the phase equation given by Passot and Newell [4]. The initial state is

$$\psi(x,y,0) = \frac{f(x,y)}{1 + \frac{f^2(x,y)}{\xi}}, \qquad (25)$$

where

$$f(x,y) = \sqrt{r}\,\cos(\alpha/2), \qquad (26)$$

where r and α denote the polar coordinates. The evolution in initial stages is shown in [Figs. 13(a) and 13(b)]. The growth of +1/2 disclination is clear, but already by $t = 10$ the effect

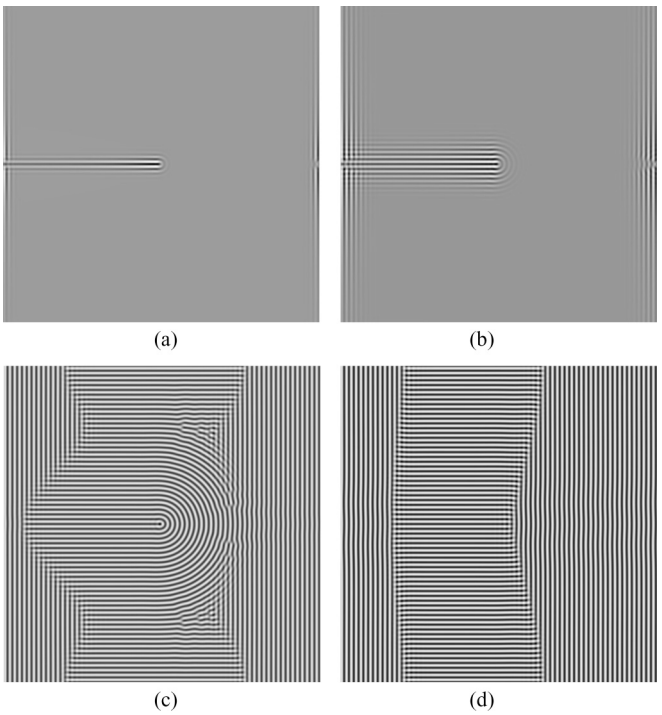

FIG. 13. Generation and evolution of a convex disclination using the initial state of Eqs. (25) and (26). Panels show the patterns at different times: (a) $t = 6$, (b) $t = 30$, (c) $t = 300$, and (d) $t = 15\,000$.

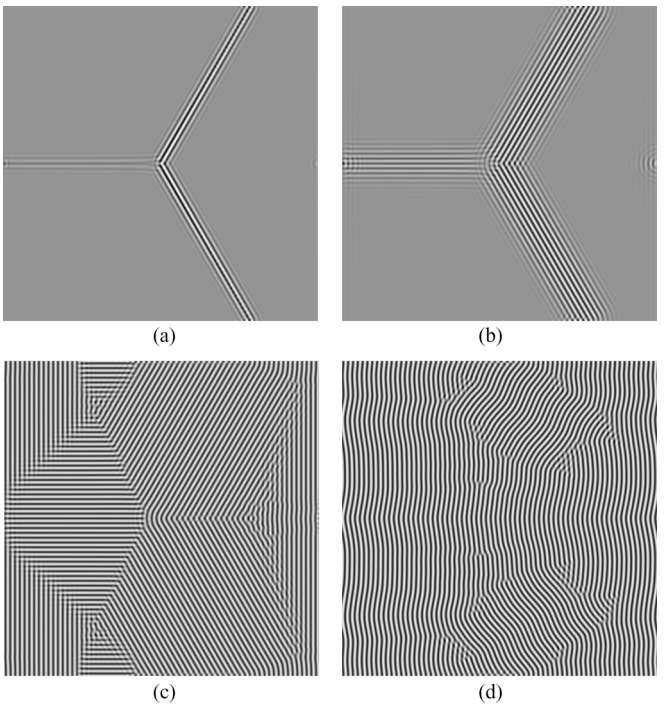

FIG. 14. Generation and evolution of a concave disclination using the initial state of Eqs. (25) and (27). Panels show the patterns at different times: (a) $t = 6$, (b) $t = 30$, (c) $t = 300$, and (d) $t = 90\,000$.

of boundary conditions begins to emerge. By $t = 300$ [see Fig. 13(c)] the boundary induced domains begin to dominate and one is left with two domains with one containing the disclination. The evolution is largely due to motion of domain walls and generation and annihilation of dislocations. At $t = 15\,000$ [see Fig. 13(d)] disclination is absorbed by the vertical domain. At this point the evolution becomes very slow as it requires motion of walls between perpendicularly aligned domains. Their motion occurs as long as the walls have curvature. The curvature becomes zero with evolution and thereafter a stable configuration is reached. The mechanism of motion is again through dissociation of stripes in the vicinity of the wall into spots.

C. −1/2 disclination

Next we present an initial state which gives rise to a concave $-1/2$ disclination. The state is given by using the following $f(x,y)$ in Eq. (25):

$$f(x,y) = r^{3/2}\cos(3\alpha/2). \tag{27}$$

This form is also suggested by the static solution of the phase equation [4]. The emergence of the disclination is clearly seen in Figs. 14(a) and 14(b). The boundary-induced domains begin to impinge on the disclination structure at $t = 300$ [see Fig. 14(c)]. This leads to formation of several domains with sharp walls and some melted triangular regions [see Fig. 14(c)]. The wall which results in connection of parallel stripes on the opposite sides of the domain move fastest causing the shrinking of the intervening domain. Then there are $\pi/2$ walls and low-angle dislocation-dominated walls which make the further evolution very slow. For the wall along the x axis the stripes from two sides make equal angles which allow reconnections. Here also after the intermediate evolution one is left with two domains with $\pi/2$ walls and low-angle dislocation-dominated walls. The long-time evolution is governed by generation of waviness in stripes through diffusive transport of curvature and rotation of walls along with generation of new regions of dislocations [see Fig. 14(d)].

D. Saddle

Finally, we generate a saddle configuration which is a disclination with winding number -1. The initial state [see Fig. 15(a)] used for this is

$$\psi(x,y,0) = \frac{x^2 - y^2}{2}\exp(-|x^2 - y^2|/\alpha). \tag{28}$$

This simulation uses zero-flux boundary conditions in place of periodic boundary conditions used above. This forces stripes to be perpendicular to the boundary which leads to a geometrical frustration for patterns in a square. Since the large gradient occurs along the lines $y = \pm x$, one sees growth of stripes along the diagonals and a rapid emergence of four domains with four domain walls, Fig. 15(b). The winding number of the pattern is -1, which is compatible with the boundary conditions. Here the interior walls have no frustration and quickly relax to two large domains with stripes oriented along diagonals, Fig. 15(c). Further, boundaries force another set of walls at the edges and defective regions in the corner. The inner domain grows till one is left with defects only near the edges, Fig. 15(d). No substantial coarsening occurs thereafter as this would require rotation of stripes of a large domain.

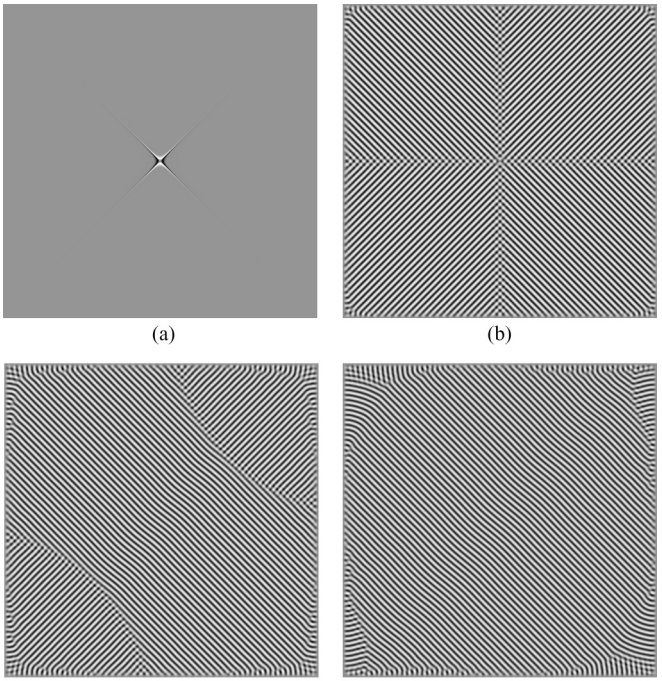

FIG. 15. Generation and evolution of a saddle on a 1025×1025 lattice with $\Delta x = \pi/8$ using the initial state of Eq. (28). Panels show the patterns at different times: (a) $t = 0$, (b) $t = 300$, (c) $t = 12\,000$, and (d) $t = 27\,000$.

VI. CONCLUSIONS

In this paper we have studied the time evolution of stripe patterns through numerical studies of the Swift-Hohenberg equation. Though a lot of work on the coarsening of stripe patterns has been reported, this system has many different features due to the nature of its order parameter which need further understanding. Here we have studied initial states which together with boundary conditions produce simple configurations and allow study of various defects in relative isolation. This approach yields qualitative and quantitative results which we summarize below.

(i) The most common defects are domain walls followed by dislocations and disclinations. Disclinations annihilate the fastest as generically the boundary conditions around them are not compatible with their topological requirement.

(ii) Domain walls are characterized by two angles that the stripes on two sides make with the wall. The walls with one of the angles near $\pi/2$ are fairly common as they are energetically favored.

(iii) We see two distinct mechanisms for domain relaxation. The first process involves dissociation of portions of stripe near the wall into spots to which a stripe from the other side connects and advances. This process requires some curvature in the wall. For example, this mechanism operates in the annihilation of domains that are enclosed by a larger domain. Such domains annihilate rather rapidly with wall speeds insensitive to their local curvature. An interesting factor which slows this process drastically is incommensuration. The frustration of the process is released by the formation of dislocations.

(iv) The second mechanism occurs by reconnection of stripes across the wall through curved segments. This process is generically frustrated in the sense that it leaves a string of dislocations. The local stripe curvature also diffuses making stripes progressively wavy. The average stripe curvature shows a nonmonotonic dependence on time.

(v) The above mechanism is considerably slower and in many situations is not completed for as long as we have observed. The defected regions slowly diffuse, rotate, and even reappear at other locations. The defect numbers, excess free energy, and stripe curvature fluctuate with time around some base values.

(vi) The motion of a straight and perturbed front was studied and its velocity tracked. Results matched very well with the theoretical predictions [38,39].

(vii) A variety of isolated topological defects were generated and the effect of boundaries on their stability examined. Their annihilation leads to dislocations and domain walls.

In the earlier work in which coarsening was studied with random initial conditions, rather definite scaling laws were found for the correlations of the stripe order and the orientational order. Here we find that dynamics of isolated defects is quite different and dependent on several features associated with overall configuration and presence of other defects.

ACKNOWLEDGMENTS

We thank S. Puri, R. Rajaraman, R. Mehrotra, and M. C. Cross for many enlightening discussions during the course of this work. A.K.T. is supported by a fellowship from CSIR, India and D.K. is supported as a Raja Ramanna Fellow by DAE, Government of India.

[1] M. C. Cross and H. Greenside, *Pattern Formation and Dynamics in Nonequilibrium Systems* (Cambridge University Press, Cambridge, UK, 2009).
[2] R. Hoyle, *Pattern Formation: An Introduction to Methods* (Cambridge University Press, Cambridge, UK, 2006).
[3] M. C. Cross and P. C. Hohenberg, Rev. Mod. Phys. **65**, 851 (1994).
[4] T. Passot and A. C. Newell, Physica D **74**, 301 (1994).
[5] N. M. Ercolini, R. Indik, A. C. Newell, and T. Passot, J. Nonlinear Sci. **10**, 223 (2000).
[6] J. Swift and P. C. Hohenberg, Phys. Rev. A **15**, 319 (1977).
[7] H. S. Greenside and W. M. Coughran, Jr., Phys. Rev. A **30**, 398 (1984).
[8] H. R. Schober, E. Allroth, K. Schroeder, and H. Müller-Krumbhaar, Phys. Rev. A **33**, 567 (1986).
[9] K. R. Elder, J. Viñals, and M. Grant, Phys. Rev. A **46**, 7618 (1992).
[10] G. H. Gunaratne, Q. Ouyang, and H. L. Swinney, Phys. Rev. E **50**, 2802 (1994).
[11] C. Sagui and R. C. Desai, Phys. Rev. E **49**, 2225 (1994).

[12] M. C. Cross and D. I. Meiron, Phys. Rev. Lett. **75**, 2152 (1995).
[13] Q. Hou, S. Sasa, and N. Goldenfeld, Physica A **239**, 219 (1997).
[14] J. J. Christensen and A. J. Bray, Phys. Rev. E **58**, 5364 (1998).
[15] D. Boyer and J. Viñals, Phys. Rev. E **63**, 061704 (2001).
[16] D. Boyer and J. Viñals, Phys. Rev. E **64**, 050101(R) (2001).
[17] D. Boyer and J. Viñals, Phys. Rev. E **65**, 046119 (2002).
[18] H. Qian and G. F. Mazenko, Phys. Rev. E **67**, 036102 (2003).
[19] H. Qian and G. F. Mazenko, Phys. Rev. E **69**, 011104 (2004).
[20] E. A. Jagla, Phys. Rev. E **70**, 046204 (2004).
[21] H. Ohnogi and Y. Shiwa, Phys. Rev. E **84**, 011611 (2011).
[22] A. J. Bray, Adv. Phys. **43**, 357 (1994).
[23] A. Onuki, *Kinetics of Phase Transitions* (Cambridge University Press, Cambridge, UK, 2002).
[24] *Kinetics of Phase Transition Dynamics*, edited by S. Puri and V. K. Wadhawan (CRC Press, Boca Raton, FL, 2009).
[25] G. Toulouse and M. Kléman, J. Phys. Lett. **37**, 149 (1976).
[26] N. D. Mermin, Rev. Mod. Phys. **51**, 591 (1979).
[27] H.-R. Trebin, Adv. Phys. **31**, 195 (1982).
[28] B. G. Chen, G. P. Alexander, and R. D. Kamien, Proc. Natl. Acad. Sci. USA **106**, 15577 (2009).
[29] D. R. Nelson and B. I. Halperin, Phys. Rev. B **19**, 2457 (1979).
[30] J. Toner and D. R. Nelson, Phys. Rev. B **23**, 316 (1981).
[31] K. Kawasaki, M. C. Yalabik, and J. D. Gunton, Phys. Rev. A **17**, 455 (1978).
[32] S. Puri, K. R. Elder, and R. C. Desai, Phys. Lett. A **142**, 357 (1989).
[33] S. Puri, Phys. Rev. A **43**, 7031 (1991).
[34] M. Suzuki, Prog. Theor. Phys. **56**, 77 (1976); **56**, 477 (1976).
[35] K. R. Elder and M. Grant, J. Phys. A: Math. Gen. **23**, L803 (1990).
[36] L. A. Segel, J. Fluid Mech. **38**, 203 (1969).
[37] A. C. Newell and J. A. Whitehead, J. Fluid Mech. **38**, 279 (1969).
[38] G. Dee and J. S. Langer, Phys. Rev. Lett. **50**, 383 (1983).
[39] W. van Saarloos, Phys. Rev. A **39**, 6367 (1989); C. Storm, W. Spruijt, U. Ebert, and W. van Saarloos, Phys. Rev. E **61**, R6063 (2000).
[40] J. Hoshen and R. Kopelman, Phys. Rev. B **14**, 3438 (1976); H. Gould and J. Tobochnik, *An Introduction to Computer Simulation Methods, Part 2* (Addison-Wesley, Reading, MA, 1988).
[41] M. C. Cross, Phys. Rev. A **25**, 1065 (1982).